Comma Cloud Development and Associated Rapid Cyclogenesis over the Gulf of Alaska: A Case Study Using Aircraft and Operational Data*

STEVEN BUSINGER

Department of Marine, Earth, and Atmospheric Sciences, North Carolina State University, Raleigh, North Carolina

BERNARD WALTER

NOAA/Pacific Marine Environmental Laboratory, Seattle, Washington

(Manuscript received 13 April 1987, in final form 16 November 1987)

ABSTRACT

The NOAA P-3 aircraft was used to collect data in a genesis region for mesoscale comma clouds over the Gulf of Alaska. Aircraft measurements in the genesis region showed that rainbands with spacings of 65–75 km and orientations along the mean wind shear were present. Possible mechanisms for the formation of the rainbands, including conditional symmetric instability (CSI) and modified wave-CISK were investigated, but the data did not allow the formation of the rainbands to be conclusively ascribed to a particular mechanism. The existence of low static stability in the genesis region was also documented and its role in mesoscale comma-cloud development explored.

Careful analysis of images from NOAA polar orbiter and GOES satellites together with synoptic analyses made it possible to trace the life cycles of several mesoscale comma clouds as the genesis region moved across the Gulf of Alaska. As the genesis region approached a preexisting polar frontal cloud band, a wave cyclone formed on the front and absorbed one of the comma clouds. The resulting cyclone central pressure dropped 25 mb in 12 hours. The intensity of this development was underestimated by operational forecast models.

1. Introduction

A flight was carried out on 12 March 1985 by the NOAA P-3 aircraft to gather data in a genesis region for mesoscale comma clouds ("genesis region" for short) over the Gulf of Alaska. The purpose of the flight was to document the environment in which these subsynoptic scale features develop. Satellite imagery and synoptic analyses were then used to document the formation of four comma-cloud systems from the genesis region and their interactions with a polar-front cloud band during the following 24 hours. The purpose of this research is twofold: (i) to examine in some detail the thermodynamic and dynamic environment in which the comma clouds formed, and (ii) to examine their role in initiating synoptic-scale rapid cyclogenesis. The term "comma cloud" (short for comma-shaped cloud system) is used in this paper to refer to mesoscale cyclonic disturbances that form in polar airmasses north or poleward of the polar front. Comma clouds typically have diameters of 500 to 1000 km as seen in the satellite imagery and are essentially nonfrontal in nature (Reed 1979; Mullen 1979).

Previous observational studies of comma clouds over the Eastern Pacific Ocean have shown that these disturbances form in regions of enhanced tropospheric baroclinicity, usually in the vicinity of preexisting frontal boundaries and on the cyclonic shear side of upper-tropospheric jet streams (Reed 1979; Mullen 1979; Reed and Blier 1986a,b). The distinctive comma-shaped cloud pattern seen in satellite imagery is coincident with a region of differential positive-vorticity advection, and usually forms from a merging of convective clouds during the incipient stage of development. Mesoscale analyses of comma clouds show that they contain rainbands often of a convective character (Businger and Hobbs 1987). In stronger cases, comma clouds may develop mesoscale advection and precipitation patterns commonly associated with fronts (Locatelli et al. 1982).

In reviewing the literature on the interaction of comma clouds with polar fronts it is evident that a variety of interactions have been documented. When comma clouds approach polar-front cloud bands rapid cyclogenesis can occur (Anderson et al. 1969; Zillman and Price 1972; Carleton 1985). In cases where the proximity is not so close (greater than 7° latitude), a wave may be excited on the polar front, and a typical midlatitude cyclone may develop, and remain inde-

* Contribution No. 907 from NOAA/Pacific Marine Environmental Laboratory.

Corresponding author address: Bernard Walter, Pacific Marine Environmental Lab/NOAA, 7600 Sand Point Way NE, Seattle, WA 98115.

pendent of the comma cloud throughout its history. In cases of closer proximity (less than 7° latitude), the comma cloud often merges with the frontal wave in a process that has been termed "instant occlusion", in which the comma cloud provides the occluded front, and the frontal wave provides the warm and cold fronts to the storm (Anderson et al. 1969). After the instant-occlusion process these storms appear identical to classical occluded systems in the cloud signatures seen on satellite imagery, but may exhibit extremely rapid pressure falls (Mullen 1983). Since they generally occur over oceans, few case studies of the interaction of comma clouds and polar fronts have had mesoscale observational data available. Mesoscale analysis by Locatelli et al. (1982) of three comma clouds that affected the Washington coast showed that the advection and precipitation patterns associated with the comma clouds and polar fronts remained independent, even though they may have appeared to merge when viewing standard operational data. Browning and Hill (1985) used mesoscale data over Great Britain to describe the circulation pattern in a case where a polar trough interacted with a polar front. The key elements of a conceptual model developed by the authors are (i) a moist, relatively warm, low-level jet associated with the polar trough, referred to as the polar trough conveyor belt, and (ii) a major upper level jet streak associated with the polar front, referred to as the polar-front conveyor belt.

In this case study, research aircraft data were available over the Gulf of Alaska, a region almost devoid of standard operational data. Therefore, this dataset presents a special opportunity to examine the environment in which a series of mesoscale comma clouds evolved. In section 2, aircraft and satellite data are used to analyze the mesoscale characteristics of the genesis region. In section 3 synoptic analyses depicting the evolution of the wave cyclone are presented. The influence of low values of lifted indices and surface sensible-heat and latent-heat fluxes on the synoptic-scale development are discussed in section 4. Summary and conclusions are presented in section 5.

2. Mesoscale analysis of a genesis region for comma clouds using aircraft and satellite data

Figure 1 shows two infrared satellite images taken by NOAA polar orbiting satellites. At 1800 UTC 12 March 1985 (Fig. 1a) the convective feature discussed below and sampled by the NOAA P-3 aircraft can be seen as a region of bright convective clouds in the vicinity of 50°N, 160°W. It has been noted (Anderson et al. 1969; Reed 1979) that an area of enhanced convection in a cold air mass is a signature of the genesis stage of comma clouds. An early indication of the presence of an upstream upper level disturbance was seen as a shift in the 500 mb wind from a southwesterly to a westerly direction at St. Paul Island (57°12′N, 170°20′W) at 1200 UTC 12 March. Satellite coverage showed that the convective activity initially (near 0000 UTC 12 March 1985—not shown) appeared as an increase in the depth of convection of a region of open mesoscale cellular convection near 175°W. These cells then became organized into a quasi-banded structure (labeled A in Fig. 1) during the latter half of 12 March. A larger convective system (labeled B in Fig. 1a) developed into a small cyclonic vortex with a comma cloud shape (labeled B in Fig. 1b). An interesting feature which persisted from near 0000 UTC 12 March until after 0000 UTC 13 March is a distinct region of suppressed convection to the east of the NE–SW oriented enhanced convective bands (A) referred to above. This relatively clear area may be related to the post-frontal subsidence associated with the preexisting polar front.

The NOAA P-3 Orion research aircraft was used to collect flight-level and Omega dropwindsonde data in the genesis region during the period 2200 UTC 12 March to 0400 UTC 13 March 1985. The aircraft primarily sampled in the convective region labeled A in Fig. 1. The flight track and the locations of deployment of the dropwindsondes are given in Fig. 2. After reaching the location of the second dropwindsonde, the aircraft performed a stepped descent from 6000 m to 300 m, and sampled the atmosphere at this level along line XY in Fig. 2. The aircraft then returned to ~6000 m to the location of the third dropwindsonde release, and turned southwest to the location of the fourth dropwindsonde. Dropwindsondes 4 through 9 (number 7 failed) were released along the line labeled PQ in Fig. 2, and dropwindsondes 10 through 12 were released along a line to the southeast. At 52°N latitude the aircraft turned west to release dropwindsonde 13 (failed) and 14, the aircraft then turned east and then north to release dropwindsondes 15 and 16 along 150°W longitude.

A series of convective rainbands (labeled R1–R5 in Fig. 3a) were encountered during the low-level portion of the flight. Bands R4 and R5 were the most intense while R1–R3 were much weaker. The rainbands were oriented with their lengths north–south, while the flight track was east–west at this time. The locations of the rainbands were determined visually from the aircraft, from the radar and from the signatures of precipitation in the downward-pointing infrared radiometer observations. The wavelength of the rainbands (the distance from the center of the radar echo of one rainband to the center of the radar echo of the next rainband) was ~60–75 km, and their average width ~20 km. The cloud turrets associated with deep convection in the rainbands were observed to extend above the upper flight level (~450 mb).

Figure 4a is a photograph of rainband R2, showing the linear organization of the cumuliform clouds. The radar-reflectivity pattern associated with rainband R4 is shown in Fig. 4b. Regions of higher reflectivity (>25

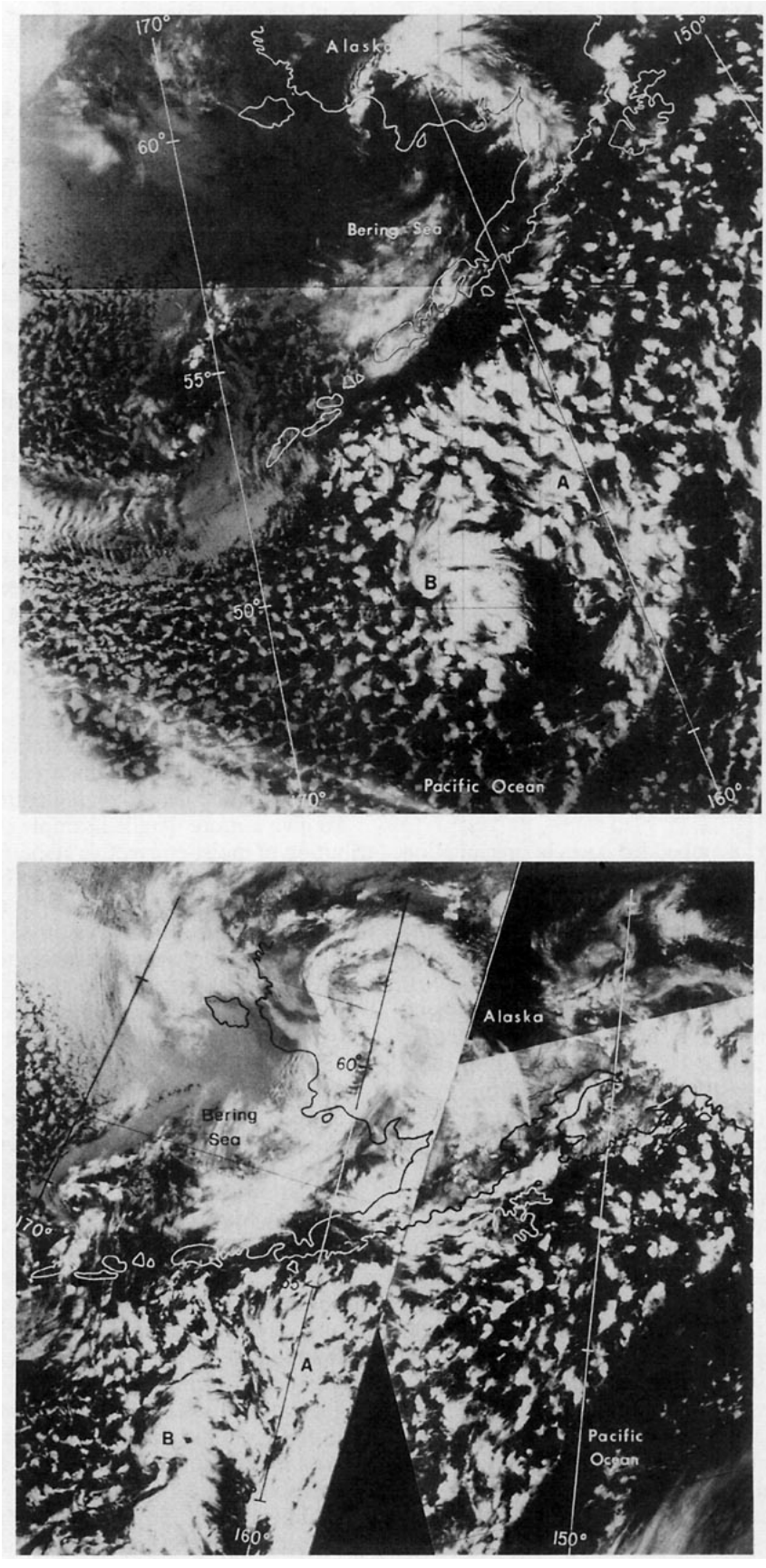

FIG. 1. NOAA-6 infrared-satellite images of an incipient comma cloud at a) 1800 UTC 12 March 1985, and b) 0000 UTC 13 March 1985. Locations labeled A and B are referred to in the text.

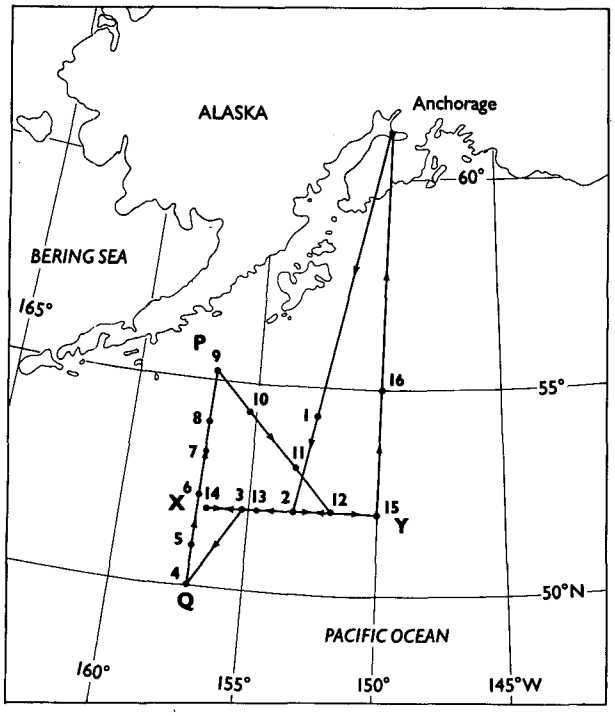

FIG. 2. Flight track and location of dropwindsonde releases on 12–13 March 1985. XY and PQ are the projection lines for the cross sections shown in Fig. 3.

dBZ) are indicative of embedded cores of precipitation within rainbands (Businger and Hobbs, 1987).

Using satellite data, an advection velocity of 15 m s^{-1} was determined for the convective bands in the genesis region. Vertical cross sections were then constructed (Fig. 3), and the advection velocity was used to adjust the location of the flight-level and dropwindsonde data long line XY in Fig. 2 to a common time of 2200 UTC on March 12. Figures 3a and 3b show cross sections prepared from the dropwindsonde and aircraft traverses along line XY. The rainband locations shown at the bottom of Fig. 3 are consistent with the time–space conversion.

Figure 3a shows isotachs of the v-component of the wind (the component normal to this east–west cross section). The isotachs show significant shear in the v-component, especially in the western half of the section, indicating that synoptic-scale baroclinicity was present. It is evident from the backing of the wind with height (shaded region in Fig. 3b) that cold-air advection was present above ~700 mb across the cross section.

The vertical cross section of the equivalent-potential temperature (Fig. 3b) shows this parameter decreased with increasing height in the boundary layer (<850 mb), and increased slightly between ~850 and ~500 mb, (the tropopause was at ~450 mb). This implies that the boundary-layer air was potentially unstable. A decrease in the equivalent-potential temperature of ~3°C was present from east to west in the cross section.

Figure 3c shows the north–south cross section prepared from the dropwindsonde and aircraft traverses along line PQ in Fig. 2. Isotachs in Fig. 3c show the u-component of the wind (component normal to this cross section). A moderately strong jet stream, with westerly winds up to 35 m s^{-1}, was located just below 500 mb, in the upper right-hand side of the figure. In section 3 we will comment on the role of the differential PVA associated with this feature on the location of the enhanced convection and the development of the wave cyclone. The equivalent-potential temperature analysis for the north–south cross section (not shown) showed a uniform layer of potential instability below ~850 mb and near neutral stability above 850 mb to the tropopause level (>500 mb). Horizontal gradients of equivalent-potential temperature were less than 1°C. Calculations of the divergence (not shown) indicate that the convergence of the component of the wind parallel to the plane of the cross sections was an order of magnitude larger for the east–west cross section than for the north–south cross section in Fig. 3. This is consistent with the observed north–south orientation of the rainbands. The spacing and the time interval between dropwindsonde releases on the east–west cross section were too large to adequately sample the mesoscale circulations associated with the rainbands, therefore, no attempt was made to calculate the vertical velocities and streamfunctions associated with these features.

To give a more detailed sample of the vertical distribution of moist-convective stability and moisture in the genesis region, temperature and dewpoint soundings from dropwindsondes 2, 5, 10 and 15 are shown in Figs. 5a–d, respectively. The majority of the soundings over the genesis region (except those in the northwest section of the region: soundings 6–10) show a well-mixed dry-adiabatic layer from the surface to 925–875 mb, capped by a deep moist-adiabatic layer to a height of 550–500 mb.

Soundings 2 and 15 were located at the eastern edge of convective region A. Both temperature soundings are nearly dry adiabatic from sea level to 875 mb. The layer below 925 mb (for sounding 15) and 875 mb (for sounding 2) is saturated due to moisture fluxes from the underlying ocean surface (surface fluxes of latent and sensible heat will be discussed further in section 4). The wetting of the dropwindsonde sensors in clouds during descent may have resulted in some overestimate of the dewpoint temperatures at low levels. Both soundings show a dry layer from ~850 to ~700 mb and a second moist layer from ~700 to ~600 mb, indicative of the advection of moisture at midlevels. Above 600 mb the dewpoint temperatures rapidly decreased in both soundings, perhaps as a result of postfrontal subsidence aloft.

Sounding 5 (Fig. 5b) was taken on the western edge of convective region A. This sounding was conditionally unstable from the surface to 875 mb and moist adiabatic from there to 500 mb (close to the observed

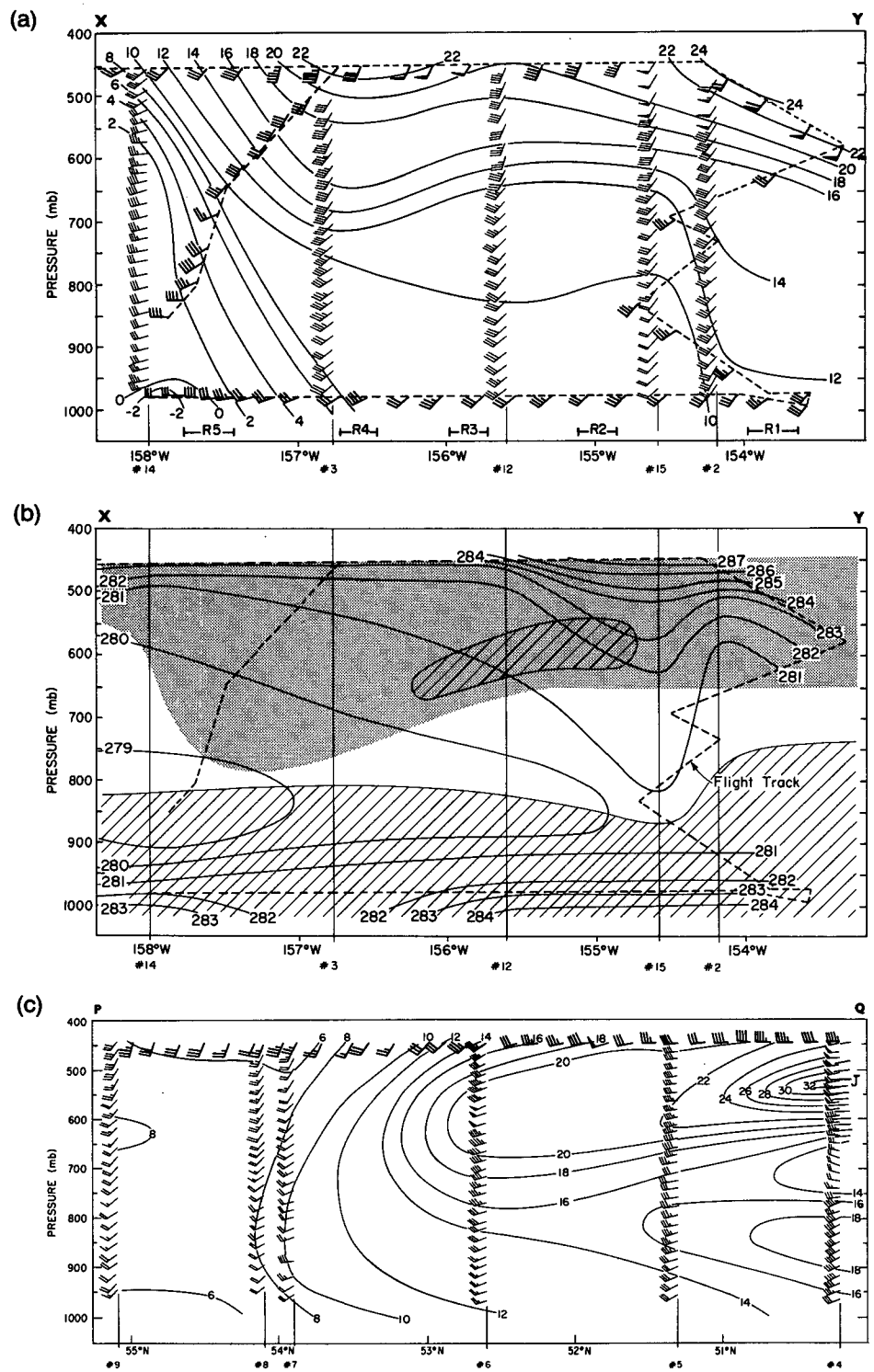

FIG. 3. Vertical cross-section along projection line XY in Fig. 2 showing: (a) Isotachs of the v-component of the wind (solid contours, contour interval 2 m s^{-1}), with the usual convention for the wind flags (barbs denote 5 m s^{-1}, triangles denote 25 m s^{-1}). R1–R5 shows the positions of the rainbands. (b) Equivalent-potential temperature (solid contours, contour interval: 2°K). Shaded region indicates backing of the wind with height, and hatched region indicates negative values of equivalent-potential vorticity. (c) As in (a) except u-component of the wind along projection line PQ in Fig. 2. "J" indicates the position of the jet core at ~500 mb. All data are adjusted to a common time of 2200 UTC 12 March.

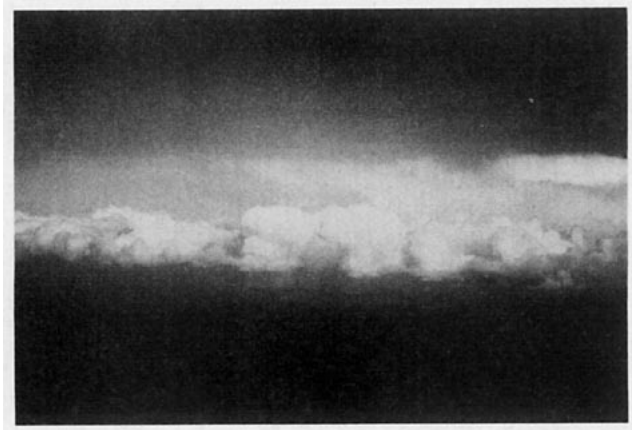

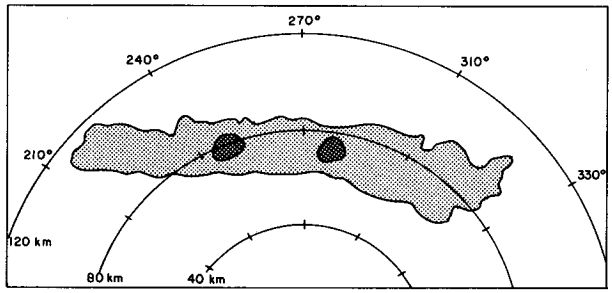

FIG. 4. (a) Photograph of organized convection in rainband R2 (see Fig. 3a) taken from the aircraft at 300 m elevation looking east at 2245 UTC 12 March. (b) Radar reflectivities in rainband R4 taken by the nose radar of the P-3 aircraft at 2330 UTC 12 March 1985. Light shading is >10 dBZ and dark shading is >25 dBZ. The semicircles show the radar range (in km) centered on the aircraft and the heading of the aircraft (in degrees).

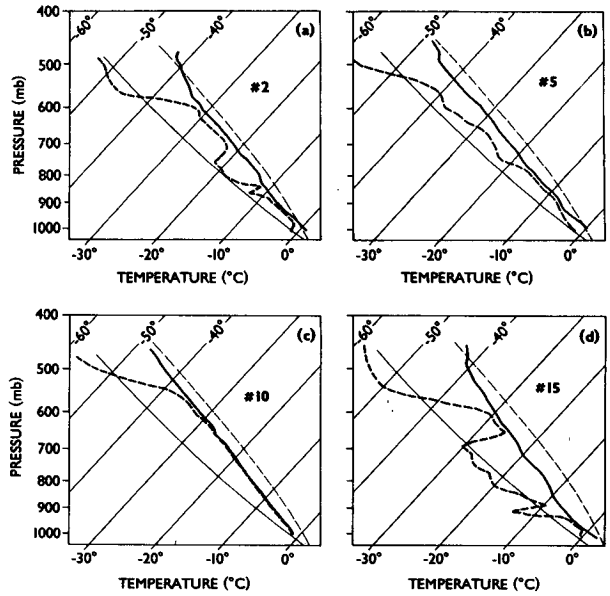

FIG. 5. Vertical soundings of temperature (heavy solid line) and dewpoint temperature (heavy dashed line) on skew-T diagrams from dropwindsonde data at locations: (a) 2, (b) 5, (c) 10 and (d) 15 in Fig. 2. Dry (light solid line) and moist (light dashed line) adiabats are indicated.

height of the convective cloud tops). The atmosphere was nearly saturated below 800 mb, gradually drying above that height. Sounding 10 (Fig. 5c) was taken to the north of the other soundings, in the middle of convective region A. This sounding shows a saturated atmosphere to 550 mb with a moist-adiabatic (neutral) lapse rate to the aircraft level at 450 mb. Soundings 5 and 10 are suggestive of an atmosphere in which deep convection has dissipated the potential instability and redistributed moisture in the vertical, resulting in the moist-neutral lapse rates.

a. Mechanisms for the rainbands

Various mechanisms have been proposed to explain the formation and maintenance of rainbands. For a review of mechanisms for rainbands associated with extratropical cyclones see Parsons and Hobbs (1983). In this subsection we will discuss several mechanisms whose predictions are most compatible with the observed characteristics of the rainbands documented in this paper.

The rainbands described in this paper were located in the vicinity of a surface trough where there were considerable variations in conditions, especially vertical windshear, over length scales of 300–500 km. A cross-section plot (Fig. 6a) of the mean wind speed relative to the convective feature A ($u' = u - u_m$) shows only a narrow region where $u' = 0$. This is also the region where the vertical shear (cold air advection) is strongest and where the two most intense convective bands (R4 and R5) were located. East of this region the shear weakens, the bands propagate faster than the mean wind ($u' \sim 5$–6 m s^{-1}) and the intensity of the convection is much weaker. These observations suggest that there is only a limited region near the trough where

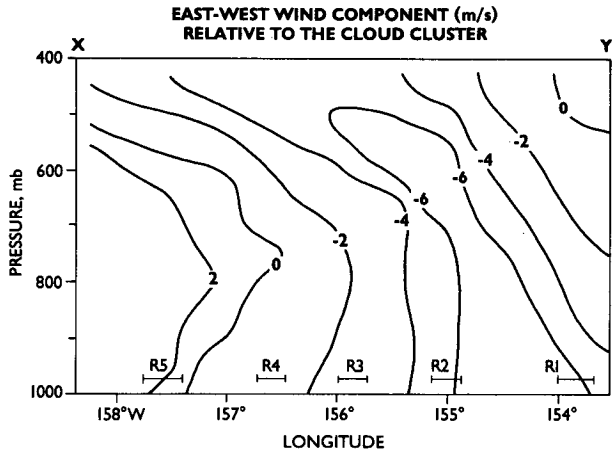

FIG. 6a. Cross-section plot along X–Y of mean u wind component relative to the speed of convective cluster A.

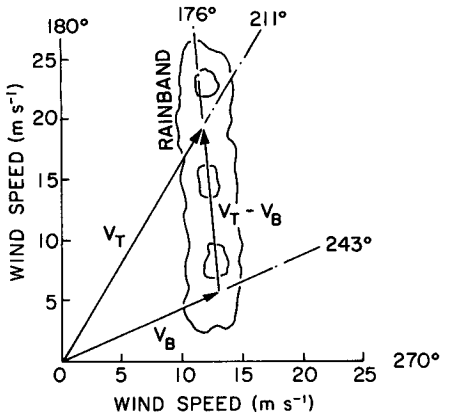

FIG. 6b. Orientation of the rainbands with respect to the shear of the mean wind for cross section X–Y. $\mathbf{V}_T$ and $\mathbf{V}_B$ are the wind velocity vectors at cloud top and cloud base, respectively, and $\mathbf{V}_T - \mathbf{V}_B$ is the wind shear vector.

conditions are such that bands will be produced. This is analogous to midlatitude squall lines where the bands of convection seem to dissipate as they propagate out of the area of vertical wind shear (Newton 1950).

To smooth the effects of ageostrophic circulations associated with the rainbands, a mean-wind profile was computed for the analyzed winds in Fig. 3a, and the vertical shear of the geostrophic wind was estimated. Figure 6b shows vectors for the mean wind at the bottom ($\mathbf{V}_B$), the top ($\mathbf{V}_T$) and the mean wind shear ($\mathbf{V}_T - \mathbf{V}_B$) for the layer in which the rainbands occurred. It can be seen that the orientation of the long axis of the rainbands was approximately parallel to the direction of the mean wind-shear vector over the depth of the cloud layer.

To summarize: the rainbands described in this paper had a mean wavelength of ~60–75 km (the distance from the center of one rainband to the center of the next rainband), and were oriented parallel to the wind-shear vector over the depth of the cloud layer. The most intense rainbands did not propagate with respect to the mean flow in which they were embedded, though weaker rainbands to their east propagated 5–6 m s^{-1} faster than the mean flow.

Two mechanisms that appear most promising in explaining the observations are conditional symmetric instability (CSI) and symmetric wave-CISK (Bennetts and Ryder 1984). Sun (1978, 1984) also investigated rainband formation using a modified wave-CISK formulation.

In favor of CSI: CSI predicts zero propagation velocity with respect to the mean wind, and an orientation of the rainband parallel to the wind-shear vector over the depth of the cloud layer, consistent with observations. The rainband spacings of 75 km are within the range predicted by CSI, and the near neutrality of the atmosphere to CSI (Fig. 5c) may imply CSI adjustment.

To further diagnose the potential for conditional symmetric instability in a saturated atmosphere, the equivalent-potential vorticity (q_e) was computed. Bennetts and Hoskins (1979) showed that regions of negative equivalent-potential vorticity will be unstable to moist-symmetric overturnings. To make these computations, a grid was constructed and the values of the wind velocities and equivalent-potential temperatures were read off the cross sections in Fig. 3. The equation for equivalent-potential vorticity can be written (Hoskins et al., 1985):

$$q_e = -g(f\mathbf{k} + \nabla_p \times \mathbf{V}) \cdot \nabla_p \theta_e \qquad (1)$$

where:

q_e equivalent-potential vorticity,
g acceleration due to gravity,
f Coriolis parameter,
$\mathbf{V}$ wind velocity,
θ_e equivalent-potential temperature,
p pressure,
∇_p three dimensional gradient operator in xyp space,
$\mathbf{k}$ unit vector in the vertical.

As discussed above, the horizontal gradients in potential temperature in the north–south direction were less than 1°C. Thus, we will limit ourselves to the two dimensions of the east–west cross section. In this case, the equivalent-potential vorticity reduces to

$$q_e = -g\left\{\frac{\partial v}{\partial x} + f\right\}\frac{\partial \theta_e}{\partial p} + g\left\{\frac{\partial v}{\partial p}\frac{\partial \theta_e}{\partial x}\right\} \qquad (2)$$

where v is the north–south velocity component of the wind.

The hatching in Fig. 3b indicates regions with negative values of equivalent-potential vorticity. The negative values below ~850 mb are largely the result of the decrease in equivalent-potential temperature with height in the lower layers of the atmosphere. Above this level, the area with negative values of equivalent-potential vorticity is unstable to moist-symmetric overturnings, while being slightly stable to moist convection. For the observed conditions either instability could have released independently. However, convective instability has a much faster growth rate than symmetric instability (the ratio of the time scales for the ascent of an air parcel being ~24/1). Satellite imagery and radar data from the aircraft indicate that the rainbands exhibited a cellular, convective nature as opposed to the continuous lines of more uniform ascent associated with CSI.

It has been suggested (Bennetts and Ryder 1984) that in regions of the atmosphere with a layer that is unstable to symmetric overturnings above a layer that is potentially unstable, symmetric instability may organize the convective release. "As potentially unstable air from the boundary layer is drawn into the upward branch of the (symmetric) roll, it will become convectively unstable" (Bennetts and Ryder 1984).

In favor of wave-CISK: A wave-CISK mechanism

would be expected to lead to significant alongband variations as the satellite observations suggest were present. The rainband spacings of 75 km are within the range predicted by wave-CISK, and the orientation of the rainbands parallel to the wind-shear vector over the depth of the cloud layer is consistent with wave-CISK.

Sun (1984) applied the wave-CISK hypothesis to the formation of mesoscale rainbands with the modification that adiabatic warming (rather than diabatic cooling) occurred in the downdraft areas. Sun found that the subsidence warming in the downdraft areas resulted in a spreading of a weak downward motion compared with the strongly concentrated upward motion and thus gave a larger wavelength of the bands than were obtained with the conventional wave-CISK assumptions. Sun also found that the horizontal temperature gradient played a large role in determining rainband movement. In the present case, the horizontal temperature gradient in the region (155.0°–156.0°W) where the strongest bands were observed was $\sim 2 \times 10^{-2}$ °C km^{-1}. This was the same magnitude as that used by Sun (1984) in his case D. He found that in the case with a temperature gradient the rainbands propagated toward the warm sector while in the case with no horizontal temperature gradient the bands propagated in both directions. Sun suggested that the existence of a horizontal temperature gradient may produce a local circulation in the subcloud layer and force the rainbands to move toward the warm side. He found a phase speed of ~ 12 m s^{-1} relative to the mean component of the wind normal to the bands in the lower convective layer.

The evidence presented by the data makes it difficult to attribute the convective band formation unambiguously to one particular mechanism. The orientation of the rainbands along the shear and the wavelength of the rainbands are characteristics consistent with both theories. The small propagation velocity with respect to the mean wind is evidence in favor of CSI, whereas the conditional instability to moist convection below ~850 mb and the cellular nature of the radar data favor the wave-CISK mechanism.

b. *Concerning the scale of the comma clouds*

Another problem that must be considered is the small scale of the comma clouds (i.e., comma cloud B in Fig. 1 is ~250 km wide and ~500 km long) and the factors responsible for the rapid deepening of these features. Satellite imagery presented in section 3 will show the development of a series of comma clouds with a very short wavelength (~500 km). A number of theoretical and numerical studies have addressed the problem of explaining the small wavelengths of cyclonic vortices in polar airmasses. Theoretical and numerical studies (Stone 1966; Staley and Gall 1977; Duncan 1977; Mansfield 1974; Blumen 1980; Satyamurti et al. 1982; Orlanski and Polinsky 1984; Orlanski 1986) show that small static stabilities at low levels (low Ri) favor a subsynoptic scale for most rapid baroclinic development.

In his composite studies of comma clouds over the Pacific Ocean, Mullen (1979) showed reduced values of the Richardson number (Ri) at low levels (<850 mb). Reed (1979), argued that the apparent discrepancy between the observed wavelength and that predicted by linear baroclinic-instability theory, may arise as a result of the difference between the highly curved mean horizontal flows in which comma clouds form, and the mean-zonal flows used in theoretical work. It will be shown (in section 3) that the flow in the case study presented here was highly curved. Numerical work undertaken by Satyamurti et al., (1982) showed that a negative curvature of the horizontal zonal winds in the lower levels of the troposphere favors growth of subsynoptic-scale waves.

Orlanski (1986) numerically investigated the evolution of meso-alpha baroclinic waves in an environment with a weakly stable vertical profile in the lower level of the atmosphere due to localized surface heating and found that this environment could support shallow, very unstable meso-baroclinic waves. He suggested that sensible heat from the surface builds up the potential energy of the dome of low-level air; when the baroclinic wave then propagates through this medium the amplitude becomes larger taking part of the accumulated potential energy and consequently reducing the intensity of the dome in the boundary layer. These waves are shallow with depths on the order of the depth of the mixed layer, have horizontal scales of a few hundred kilometers, and can organize convergence of moisture on these scales. With the addition of moisture the waves then develop into intense meso-alpha cyclones. Based on these model results (Orlanski, personal communication 1985) the aircraft flight tracks in the present study were designed to obtain information on the reduced low-level static stability in the vicinity of developing comma clouds.

To investigate the possible relationship in the present case between reduced low-level static stability and the small scale of the comma clouds seen in the satellite imagery, the Richardson number (Ri) was calculated for the east–west cross section (Fig. 3). Data from the dropwindsondes (Figs. 5a and 5c) showed that the atmosphere was nearly saturated below ~550 mb due to upward distribution of moisture by the convection. Thus, the distribution of Ri was investigated for a saturated environment and, following Bennetts and Hoskins (1979) and Durran and Klemp (1982), the equivalent potential temperature was used to calculate Ri:

$$\mathrm{Ri} = -\frac{\gamma_m}{\gamma_d \rho \theta_e}\left[\frac{\partial \theta_e}{\partial p}\right]\left[\frac{\partial v}{\partial p}\right]^{-2} \tag{3}$$

where

γ_m moist-adiabatic lapse rate,
γ_d dry-adiabatic lapse rate,
ρ density of the air.

The results of the Ri computations (Table 1) show small values of Ri below 850 mb, reflecting the low static stability in this layer. A second region of small Ri is found between ~700 and 600 mb in a region of enhanced shear of the v-component of the wind with height (Fig. 3a, longitude 156.5°W). Ri rapidly increases with height above ~500 mb. Also shown in Table 1 are values of the dry Richardson number where potential temperature instead of equivalent potential temperature was used. These results favor a subsynoptic scale for the most rapidly growing baroclinic wave (Stone 1966; Blumen 1980). Surface sensible heating provides the source of low level instability. It will be shown in section 4 that the fluxes of latent and sensible heat from the ocean surface to the atmospheric boundary layer were significant in the present case.

The Richardson number can be also used as a way of diagnosing the stability of the atmosphere to infinitesimal perturbations (Stone 1966; Bennetts and Hoskins 1979). Stone (1966) shows that symmetric instabilities dominate when $0.25 < Ri < 0.95$. The region between 700 and 600 mb (Table 1) was largely unstable to moist symmetric overturnings. (Since the above computations were made with the assumption that the atmosphere was saturated, strictly speaking, the results are only valid in regions of cloud.)

The role of latent heat release on growing polar vortices has also been the subject of a number of investigations. It is reasonable to assume that latent-heat release influenced both the wavelength and the intensity of the comma clouds observed in this case. Since it is difficult to estimate the shape of the heating profile due to latent heat release, the question of its influence on the development of the comma clouds may best be addressed through studying simulations of the storms in a mesoscale numerical model. Orlanski and Polinsky (1984) showed that weak meso-alpha cyclones (~500 km) developed for dry simulations in approximately the same geographic position as those with latent heating suggesting that the dry atmosphere may have the necessary ingredients for cyclone development but that latent heat makes the development explosive. Gall (1976) has shown that convective adjustment processes, resulting in latent heat release, tend to increase the warm temperature perturbations of baroclinic waves at midtropospheric levels, thus resulting in deeper disturbances. In our case convection associated with the comma clouds reached the tropopause. Tokioka (1973) found that the inclusion of condensational processes in a baroclinic model greatly increased cyclogenesis, while favoring the development of small-synoptic scale wavelengths. Latent heat released in this case study may have been important in determining the short wavelengths of the comma clouds.

In the next section, satellite imagery and synoptic maps of the region of the insipient comma cloud and the remnant polar front are presented.

3. Synoptic and satellite analysis of the interaction of the genesis region and the polar-front cloud band

The series of infrared satellite images taken by the Geostationary Orbiting Earth Satellite (GOES) satellite

TABLE 1. Moist and dry Richardson number for cross section XY in Fig. 3.

	Longitude						
Pressure (mb)	157.5°	157.0°	156.5°	156.0°	155.5°	155.0°	154.5°
			Moist				
500	15	9	5	4	12	14	12
550	3	4	4	4	2	3	4
600	0.7	2	4	0.7	0.4	0.7	0.7
650	1.3	0.7	1.3	0.3	1.3	1.3	1.3
700	2	0.6	0.3	2.5	35	17	0.4
750	4	1.2	1.2	3	15	16	7
800	1.6	0.3	1.6	1.8	0.6	11	0.3
850	−1	−2	−12	−9	−5	−27	2
900	−4	−3	−23	−14	−17	−37	−28
950	−6	−7	−38	−54	−76	−82	−82
			Dry				
500	19	10	5	4	11	7	26
550	10	12	9	10	4	5	5
600	3	7	14	6	1.5	5	2
650	3	4	4	4	10	13	5
700	7	5	5	14	210	71	20
750	21	11	6	25	88	46	59
800	40	33	13	30	36	67	267
850	24	11	112	76	34	200	987
900	2	2	28	19	22	50	82
950	2	9	127	88	30	39	49

shown in Fig. 7 will be used to gain an overview of the evolution of the wave cyclone and its interaction with the genesis region for comma clouds. In Fig. 7a (0300 UTC 13 March 1985) a frontal cloud band and a convective region to the west are visible. The frontal cloud band indicates the position of a remnant polar front that was left in the wake of a midlatitude cyclone that crossed the Alaska and British Columbia coastline on 10 March 1985. Two areas of bright cloud (labeled A and B in Fig. 7a) can be distinguished in the convective region to the west of the frontal cloud band. These are the same features shown in Fig. 1, and it was this general area of enhanced convection that was termed the genesis region for comma clouds earlier. The aircraft data (described in section 2) was taken primarily in the feature labeled A.

Figures 7b (0830 UTC) and 7c (1230 UTC) show the development of a wave cyclone as the genesis region approached the polar front. An occlusion cloud band (labeled W in Figs. 7c–f) developed as the wave cyclone rapidly deepened on 13 March 1985, resulting in a large comma-shaped cloud of synoptic scale in the satellite imagery. Since this comma-shaped feature is of a significantly larger scale than the smaller class of disturbance called "comma clouds" previously in this paper, the larger comma head will be referred to as the "occlusion cloud band," and its tail will be referred to as the "cold-front cloud band."

The convective region labeled A is seen to elongate and separate into two parts (relabeled A and C in Fig. 7b), and a small comma cloud (labeled D) can be seen to enter the images from the west, behind comma cloud B (Fig. 7d). In the polar-orbiting satellite imagery for 1200 UTC 13 March (not shown) the signature of deep convection was observed along the cloud band of the occlusion. This was verified by the expansion of the bright cloud along the occlusion cloud band in the GOES satellite imagery for 1230 UTC (Fig. 7c). In Figs. 7d (1830 UTC), 7e (2030 UTC) and 7f (2230 UTC) the convective region A was stretched in an east–west direction by the inflow field of the larger scale wave cyclone, while convective region C moved northeast towards Anchorage. With the aid of the enhanced resolution of the polar-orbiter satellite imagery (Fig. 8), details of the occlusion cloud band and convective systems (labeled A–D in Fig. 7) can be seen. Comma-cloud shapes are evident for the systems labeled B, C and D in Fig. 8a and a larger scale comma can be seen associated with the wave cyclone. As discussed in the previous section, it is interesting to note the very short wavelengths exhibited by the comma-cloud systems in the satellite imagery (the spacing between comma clouds D and B is ~400 km). Evidence for strong convection (labeled "c" in Fig. 8) seen along the occlusion cloud band of the cyclone was supported by ship observations of towering cumulus. During the time interval between the satellite images (Figs. 8a at 2300 UTC 13 March and 8b at 0200 UTC 14 March) the area of bright cloud in system A rapidly expanded and merged with the cloud band of the occlusion resulting in a redevelopment and the characteristic "comma" shape within the larger comma of the wave cyclone in Fig. 8b. Careful tracking of the cloud features showed that the head of the new comma cloud developed out of the inner spiral of the occlusion cloud band, while convective system A provided the tail of the comma cloud.

Horizontal maps of pressure, temperature and geopotential heights showing the synoptic evolution of the wave cyclone are presented in Figs. 9–11.

Geopotential analyses of 850 mb heights and temperatures for 0000 UTC 13 March 1985 are shown in Fig. 9a, and those for 700 mb are shown in Fig. 9b. Dropwindsonde data in both analyses show a short-wave trough, with the trough axis located near 157°N longitude and a broad swath of moderately strong westerly winds across the Northern Pacific Ocean. The lowest temperatures are located behind or west of the trough axis, with a region of cold air advection ahead of the trough axis (temperatures were plotted to the nearest °C, in some cases resulting in apparent slight inconsistencies in the temperature analyses in this section).

In Fig. 10 geopotential analyses of 500 mb heights and temperatures are shown in 12 hour intervals starting at 0000 UTC 13 March 1985. The locations of the convective systems (A–D) with respect to the position of the 500 mb trough are also shown. Dropwindsonde data in Fig. 10a show a short-wave trough, with temperatures of −45°C located along the trough axis just east of 160°W. Convective region A (shaded region in Fig. 10a) is located just east of the trough axis and the area of lowest temperatures at 500 mb. Calculations of the PVA from the height analyses show that the region of largest PVA at 500 mb is also located east of the trough axis, just north of the jetstream axis at 500 mb (~50°N) (see "J" in Fig. 3c). Comparison of the magnitude of the Laplacian of the cold-air advection and the PVA at the 500, 700 and 850 mb levels showed a contribution to upward motions (Sutcliffe 1947; Holton 1979), thus providing a favored region for development. Convective region B is located west of the trough axis, in an area of enhanced positive vorticity just north of the axis of the jetstream at 500 mb. Figs. 10b and c show the eastward movement of the trough toward the British Columbia Coast. The convective regions A, B and D stayed in constant phase with respect to the position of the trough axis, and remained just north of the axis of strongest winds at this level. Convective region C gradually moved northward out of the belt of strong westerlies. The position of the surface low-pressure center (denoted by the circled cross) was gradually overtaken by the trough axis, and rapid deepening of the surface low-pressure center ensued. By 0000 UTC 14 March a closed low appears at 500 mb and the distance between the trough axis at 500

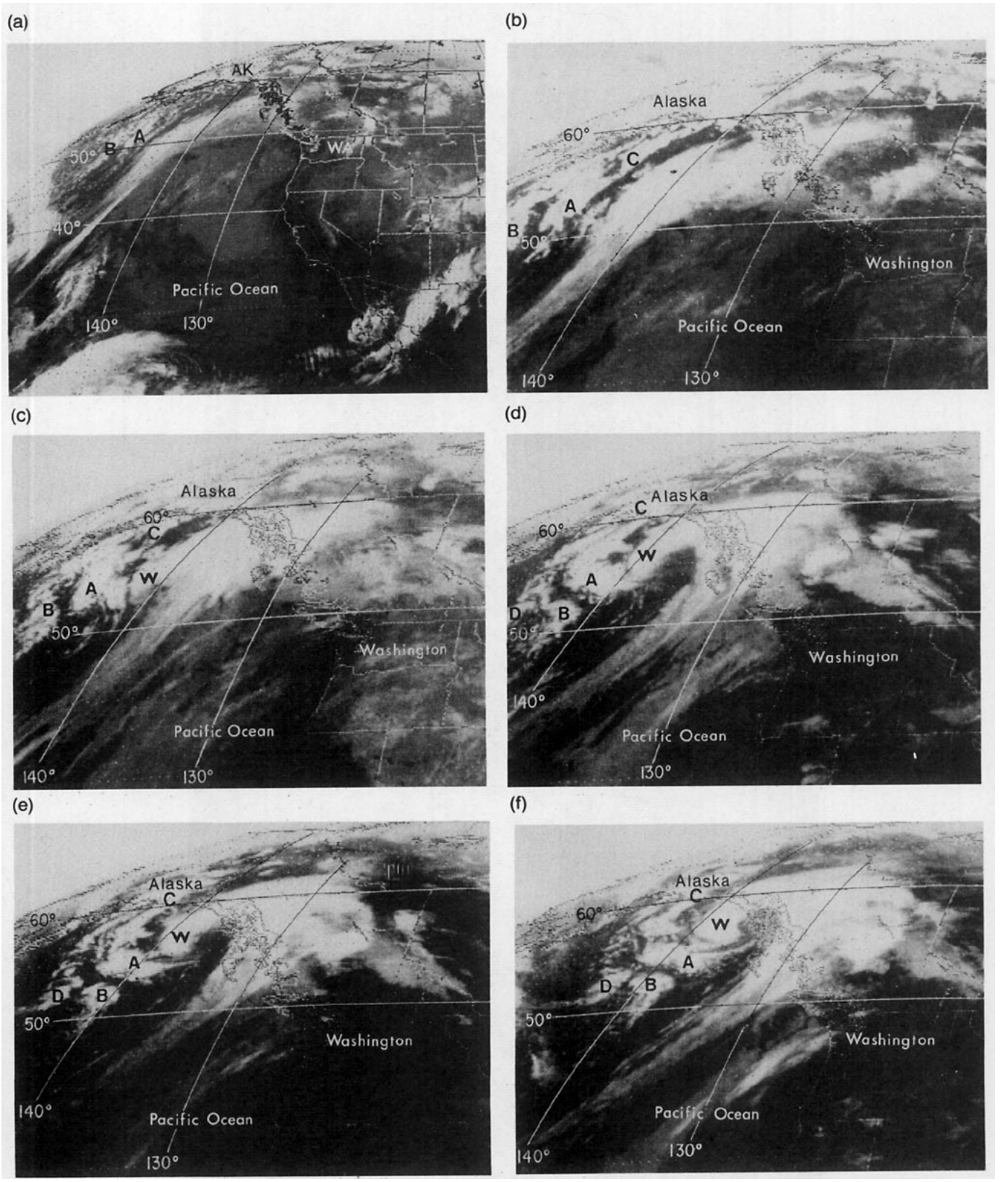

FIG. 7. Geostationary infrared-satellite images for: (a) 0300 UTC, (b) 0830 UTC, (c) 1230 UTC, (d) 1830 UTC, (e) 2030 UTC and (f) 2230 UTC 13 March 1985. Labeled areas are referred to in the text.

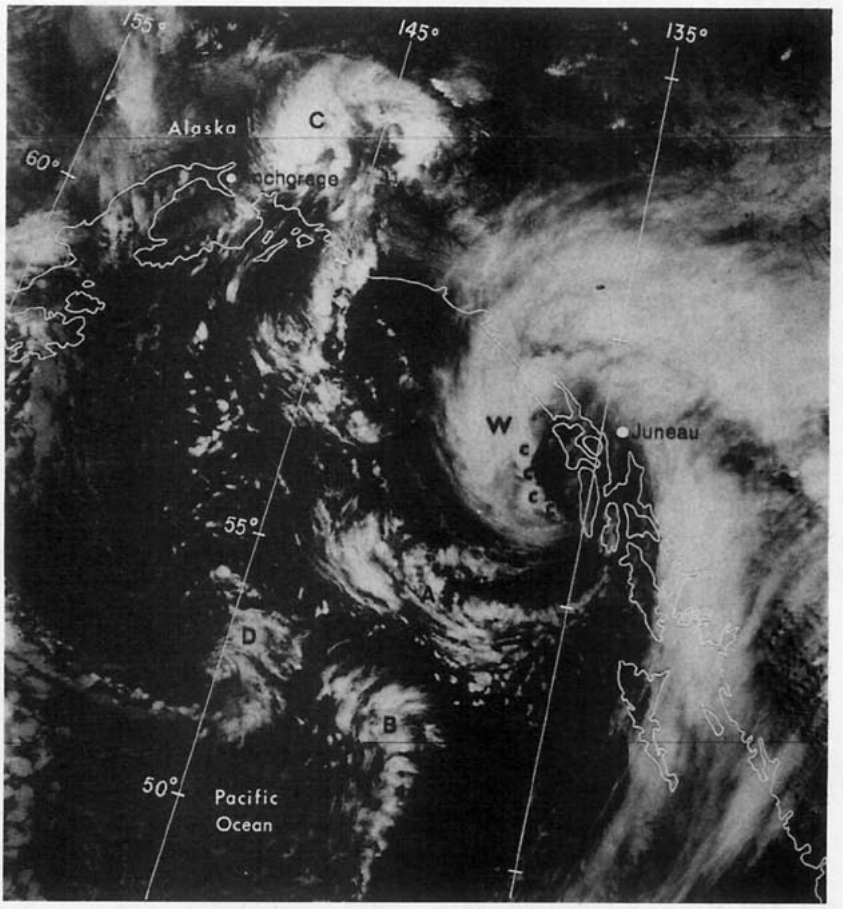
155°
145°
135°
Alaska
C
60°
Anchorage
W
Juneau
55°
A
D
B
50°
Pacific
Ocean

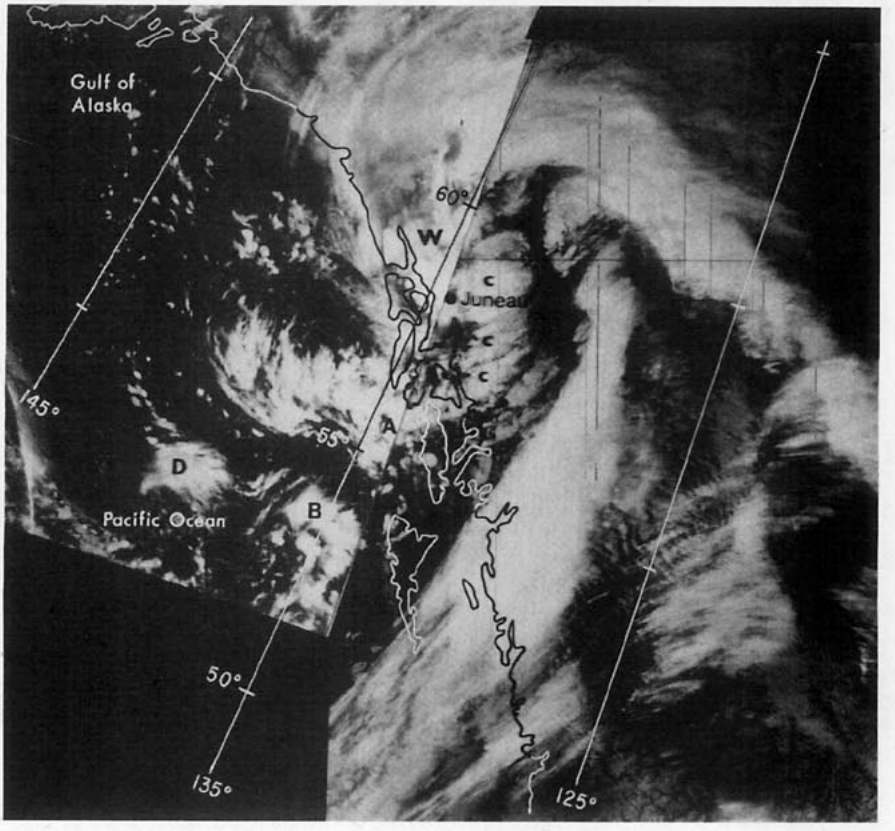
Gulf of
Alaska
60°
W
Juneau
145°
55°
A
D
Pacific Ocean
B
50°
135°
125°

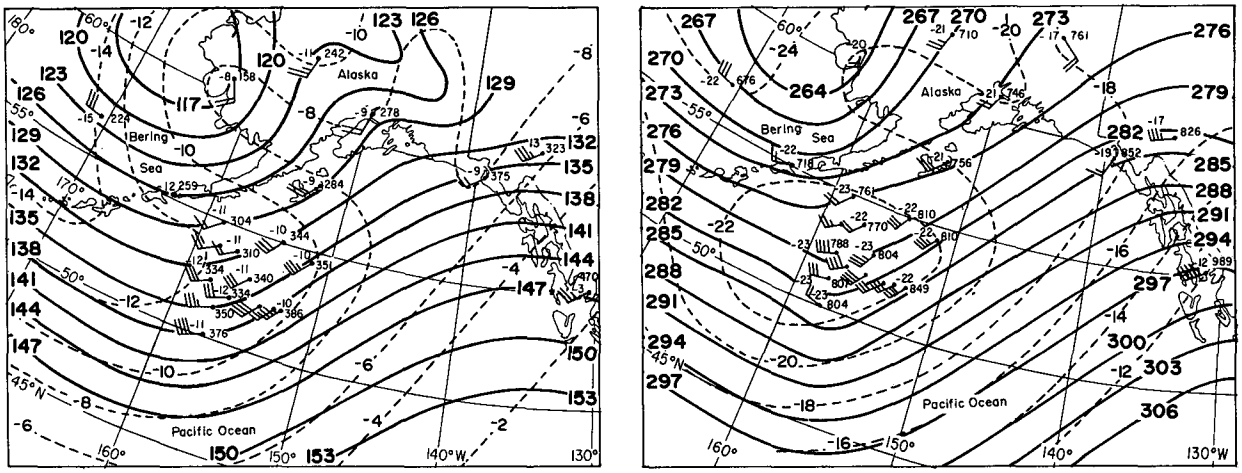

FIG. 9. Geopotential analyses for 0000 UTC 13 March 1985 for the (a) 850 mb level and (b) 700 mb level, showing heights (solid contours, interval: 30 m) and temperatures (dashed contours, interval: 2°C).

mb and the low pressure center at the surface has decreased to ~250 km.

Figures 11a–e show the evolution of the surface-pressure field in 6 hour intervals starting at 0000 UTC 13 March 1985. Figures 11a and 11b show a weak cold front south of 50°N, and a dissipating stationary front north of 50°N. These features were left in the wake of a wave cyclone that passed across the British Columbia Coast on 10 March 1985 and they are associated with the frontal cloud band seen in the geostationary-satellite images (Fig. 7). There was a slow fall in pressure in the vicinity of the low-pressure center (denoted by the L) between 0000 and 0600 UTC.

During the following twelve hours, between 0600 and 1800 UTC 13 March, the pressure fell more than 2 mb h^{-1} to a central pressure of 1002 mb at 1200 UTC (Fig. 11c), and 989 mb at 1800 UTC (Fig. 11d). There was evidence in the satellite imagery (see small "c"s in Fig. 8) that deep convection developed along the cloud band of the occlusion. By 1800 UTC the satellite imagery shows the cloud signature of a mature occluded midlatitude cyclone (Fig. 7d). Figure 11e shows the surface low-pressure center reaching the British Columbia Coast. The central surface pressure of the cyclone was ~988 mb at this time (0000 UTC 14 March).

Figure 12 shows the deepening rate of the central pressure as a function of time, and the horizontal separation between the 500 mb trough axis and the surface-low center. The most rapid deepening of the wave cyclone occurred when the separation between the 500 mb trough axis and the surface low center was between ~550 and ~350 km, consistent with baroclinic theory. Landfall of the cyclone probably inhibited further deepening after 1800 UTC 13 March.

The picture described above is consistent with the B-type development of Petterssen and Smebye (1971), and agrees with analytical results of Farrell (1982, 1984). By taking nonmodal (neutral) initial conditions, corresponding to an upper-level trough overtaking a surface depression, Farrell showed that transient growth ensues, in which the scale of the cyclogenesis is that of the seed disturbance, and is independent of the most rapidly growing normal mode. As a short-wave trough approaches a surface depression, a tilt in the resulting vertical-trough axis produces a favorable phasing of the wind and temperature distributions.

Model forecasts by NMC's Limited Area Fine Mesh (LFM) model underestimated the deepening of the cyclone by 12 mb in 24 hours. Sanders and Gyakum (1980) have also noted the tendency of the LFM to underestimate the central pressure of rapidly deepening midlatitude cyclones. Some of the discrepancy can be accounted for by insufficient upper-level data over the Gulf of Alaska, and a resulting underestimate of the amplitude of the short-wave trough at 500 mb at 0000 UTC 13 March. The maximum vorticity at 500 mb associated with the trough in the LFM analysis at 0000 UTC 13 March was 12×10^{-5} s^{-1}, whereas in our reanalysis with the aircraft data the value was 22×10^{-5} s^{-1}. Sanders and Gyakum (1980) suggest that adequate representation of the planetary-boundary layer and of the bulk effects of cumulus convection are necessary physical ingredients missing from the model.

FIG. 8. NOAA-6 infrared-satellite images showing the interaction of the developing comma clouds. (A–D) and the wave cyclone at (a) 2300 UTC 13 March 1985 and (b) 0200 UTC 14 March 1985. Lower case "c" indicates locations of enhanced convection along the occlusion cloudband (W).

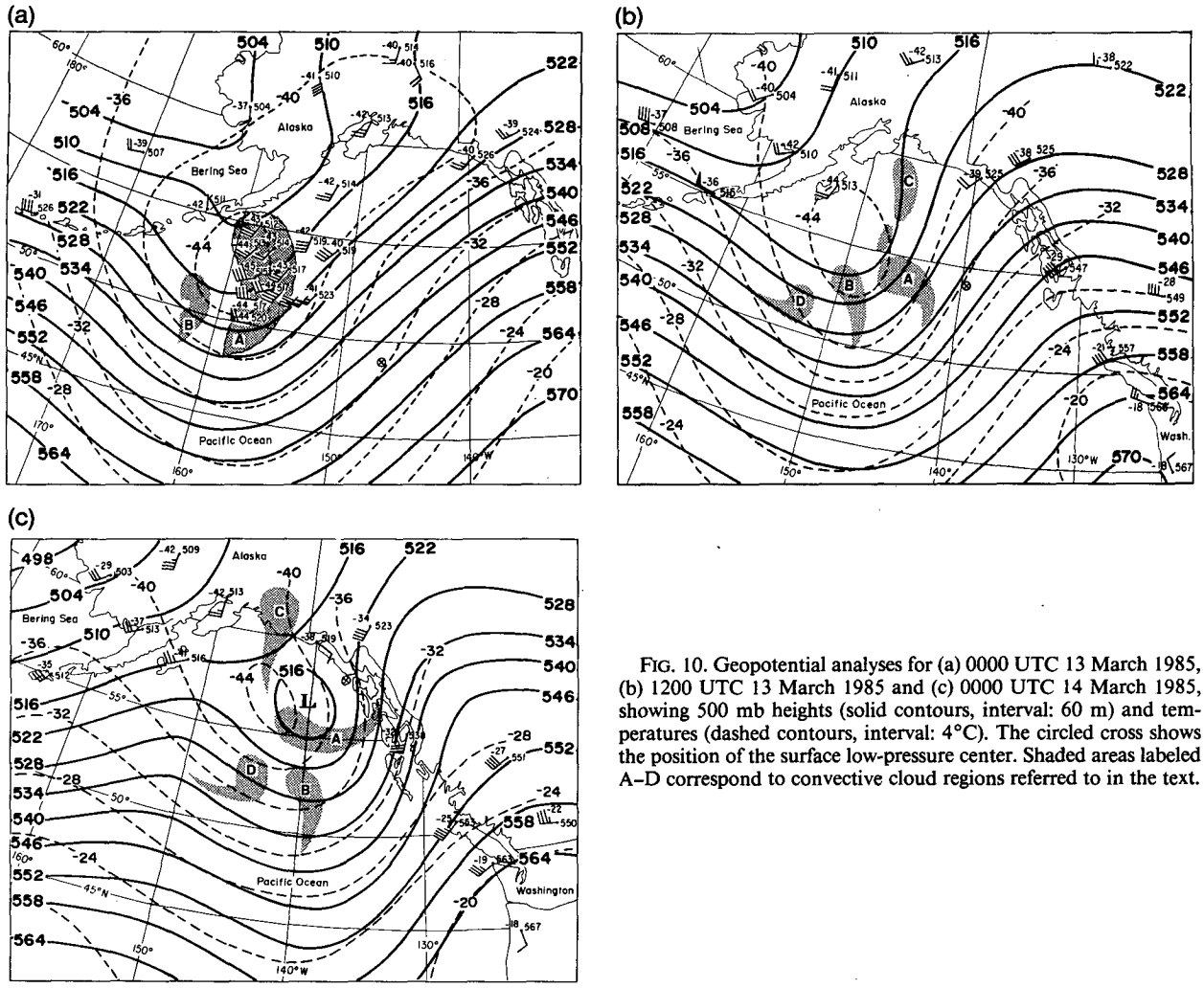

FIG. 10. Geopotential analyses for (a) 0000 UTC 13 March 1985, (b) 1200 UTC 13 March 1985 and (c) 0000 UTC 14 March 1985, showing 500 mb heights (solid contours, interval: 60 m) and temperatures (dashed contours, interval: 4°C). The circled cross shows the position of the surface low-pressure center. Shaded areas labeled A–D correspond to convective cloud regions referred to in the text.

As discussed above there was evidence of deep convection along the occlusion cloud band during the time of most rapid deepening. The relationship between the distribution of the deep convection and the development of the wave cyclone will be discussed in the next section.

Surface station data from Juneau and Sitka on the Southeast Alaska Panhandle showed very weak responses to the passage of the front associated with the wave cyclone (~2130 UTC 13 March at Juneau). However, they showed a pronounced response to the passage of the surface trough associated with the redeveloping comma cloud A. Hourly surface data from Juneau are shown in Fig. 13. The pressure trace shows a sharp fall of 25 mb in 13 hours, followed by a rapid rise in pressure beginning at ~0130 UTC March 14. Steady winds of 20 m s^{-1}, with wind gusts up to 26 m s^{-1} accompanied the passage of the surface trough associated with the comma cloud.

4. Lifted indices and sea-surface fluxes

It is known from baroclinic theory (Eady 1949) that low static stability enhances the development of baroclinic waves while reducing the wavelength of maximum growth. It was shown in section 2 that the genesis region (A and B in Fig. 1) was associated with a deep layer (to ~500 mb) of conditional instability. As the genesis region overtook the surface low center the static stability decreased in the vicinity of the low center and probably contributed to the explosive deepening of the wave cyclone (Orlanski 1986).

To examine the evolution of the thermodynamic stability during the period leading to the explosive deepening, lifted indices and surface fluxes of sensible and latent heat were computed.

The lifted index has been used in the past as an indicator of regions with the potential for development of deep convection (Reed and Albright 1986; Reed and

Blier 1986b). The lifted indices were computed on a 2° × 2° latitude–longitude grid, using values interpolated from analyzed fields of surface pressures, and special analyzed maps of surface temperature and dewpoints derived from ship and buoy data at 0000 and 1200 UTC 13 March and 0000 UTC 14 March. Grid values of the 500 mb temperatures were taken from the analyses in Fig. 10. Parcels were raised dry adiabatically from the surface to the lifting-condensation level, and then moist adiabatically to 500 mb, where the parcel temperatures were subtracted from the ambient temperatures to obtain the lifted indices.

Regions with large negative values of the lifted index in Fig. 14 were well correlated with the regions that exhibited deep convection in the satellite imagery. The area of lowest values of the lifted index at 0000 UTC on 13 March (Fig. 14a) encompasses the area of greatest convective activity (A and B in Fig. 1), and corresponds reasonably well to the region of lowest 500 mb temperatures (Fig. 10a). Fig. 14b shows the lifted indices for 1200 UTC March 13. The area of lowest lifted indices has shifted eastward with time. The region of lowest temperatures at 500 mb and the region of enhanced convection also moved eastward, following the eastward movement of the short-wave trough. At this time the negative values of the lifted index (Fig. 14b) are less than 2° longitude from the location of the surface low-pressure center (circled cross), and convection was seen to develop along the occlusion cloud band in the satellite imagery. By 0000 UTC March 14 the lifted indices in the vicinity of the surface low-pressure center reduced further (Fig. 14c) since the boundary-layer air continued to warm and moisten, and the temperature at 500 mb increased little. As discussed in section 3, the signature of strong convection could be seen along the cloud band of the occlusion and along the length of convective region A as they merged (Fig. 8). The potential for the new comma cloud to intensify was probably not fully realized as a result of the inhibiting effects of the high mountains of the British Columbia Coast on further deepening.

Surface fluxes of heat and moisture reduce the moist static stability resulting in an increased potential for convective activity in the regions of strongest fluxes. The latent and sensible heat fluxes were computed for 0000 and 1200 UTC March 13 using the bulk aerodynamic method described in Reed and Albright (1986). Only a brief summary of the results will be presented here, since the distribution of the fluxes do not appear to have directly promoted development of the wave cyclone.

The fluxes of latent and sensible heat for 0000 UTC 13 March showed moderately large values (total fluxes between 150–300 W m^{-1}) over the Northern Pacific and Gulf of Alaska (Figs. 15a and 15b), reflecting the modification of the boundary layer as dry, cold arctic air was advected from the Bering Sea over these regions. The convective region of the incipient comma cloud sampled by the flight is located in this region of enhanced fluxes. It is likely that fluxes of latent and sensible heat from the sea surface contributed to the potential instability found below ~850 mb in the cross sections (Fig. 3), the reduced values of Ri at low levels (Table 1), and the low values of the lifted indices (Fig. 14a). The fluxes were negligibly small in the vicinity of the low pressure center associated with the wave cyclone at this time.

Although some of the air over the Northern Gulf of Alaska passed to the north of the wave cyclone into Alaska (i.e., convective region C), trajectory analysis showed that the air associated with convective region A was absorbed into the wave cyclone during the merging process described in the previous section.

The fluxes of latent and sensible heat for 1200 UTC 13 March (not shown) indicated moderate surface fluxes (total fluxes up to 250 W m^{-2}) to the southwest of the surface low-pressure center and west of the cold front (a configuration that actually dampens the growth rate of baroclinic waves). These fluxes may have aided the reduction in the lifted indices for 0000 UTC March 14 (Fig. 14c).

5. Summary and conclusions

This paper documents the development and life history of several mesoscale comma clouds over the Gulf of Alaska and examines their role in initiating synoptic-scale rapid cyclogenesis. The NOAA P-3 research aircraft collected a comprehensive dataset over the Gulf of Alaska on 12 March 1985 in a region of enhanced convective activity that was a genesis region for the comma clouds. The goal of this effort was to examine the thermodynamic and dynamic environment of this genesis region.

The genesis region was associated with a cold-core trough at 500 mb (−40° to −45°C) and a region of strong forcing by differential PVA. Aircraft observations taken within the genesis region indicated that convection was organized into distinct rainbands (60–75 km wavelength), with tops extending to the tropopause. The most intense rainbands formed in a region of enhanced vertical wind shear near the trough axis, did not propagate with respect to the mean flow in which they were imbedded, and were oriented parallel to the wind-shear vector over the depth of the cloud layer. East of the trough axis the rainbands weakened as they propagated out of the region of strongest vertical wind shear, analogous to observations of midlatitude squall lines.

Two mechanisms that appear promising in explaining these observations are conditional symmetric instability (CSI) and symmetric wave-CISK. The observed rainband spacings (60–75 km), and the orientation of the rainbands parallel to the wind-shear vector

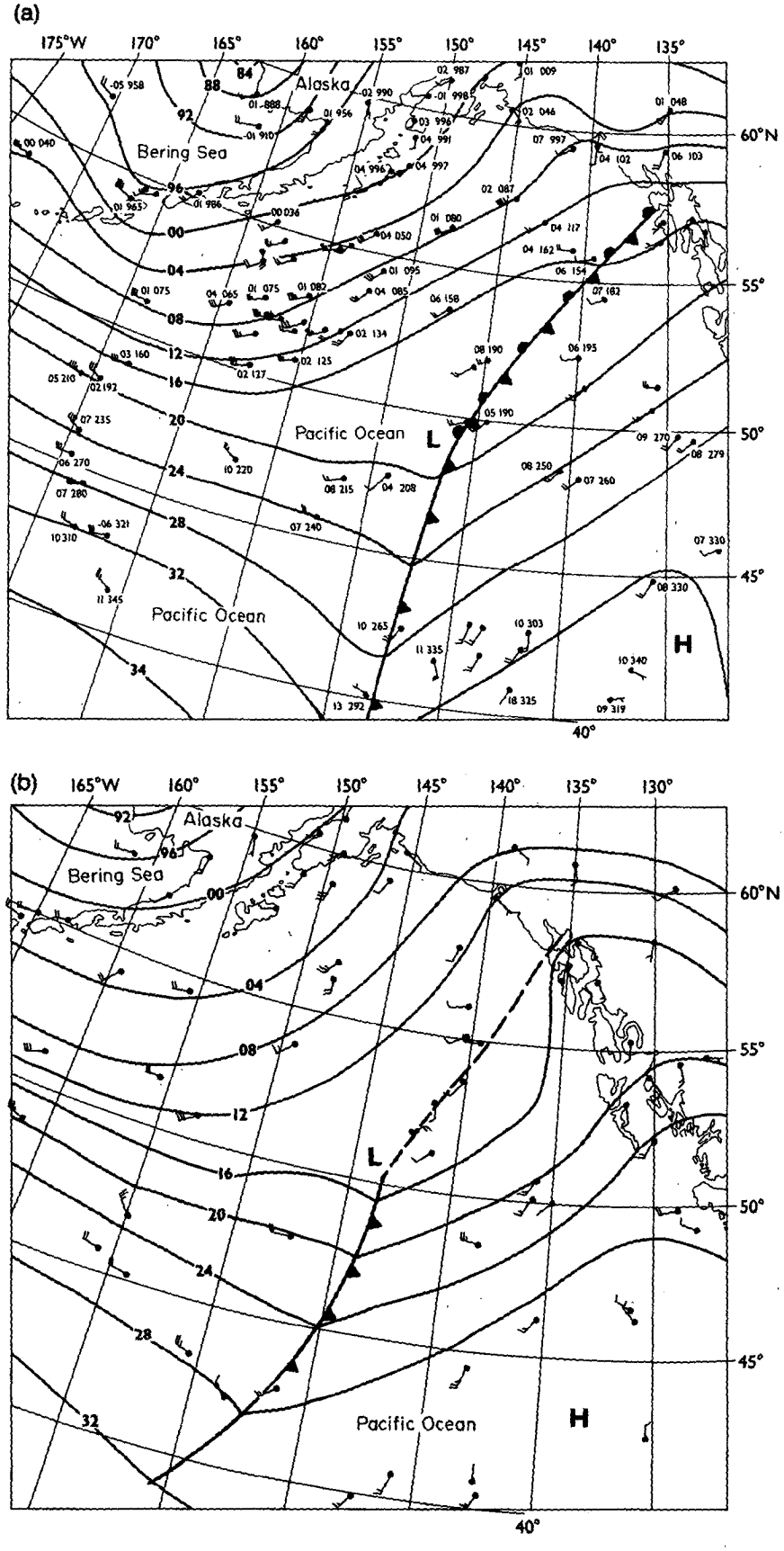

FIG. 11. Surface analyses for: (a) 0000 UTC, (b) 0600 UTC, (c) 1200 UTC and (d) 1800 UTC 13 March 1985 and (e) 0000 UTC 14 March 1985. Solid contours are surface pressure (contour interval: 4 mb).

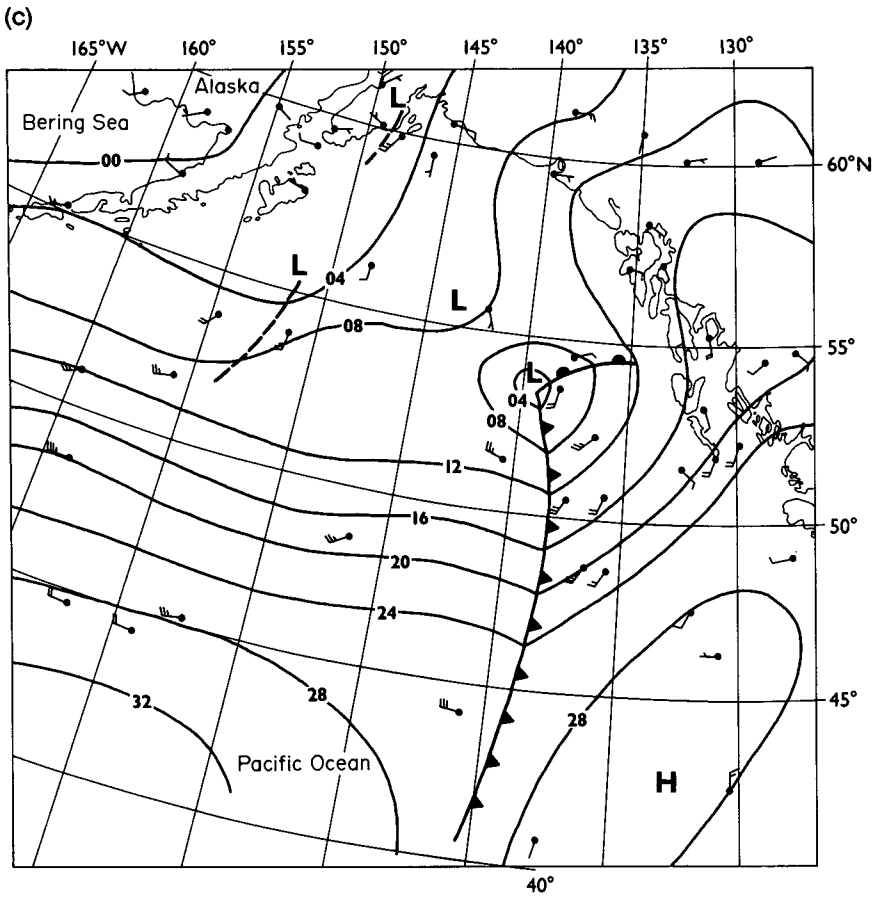

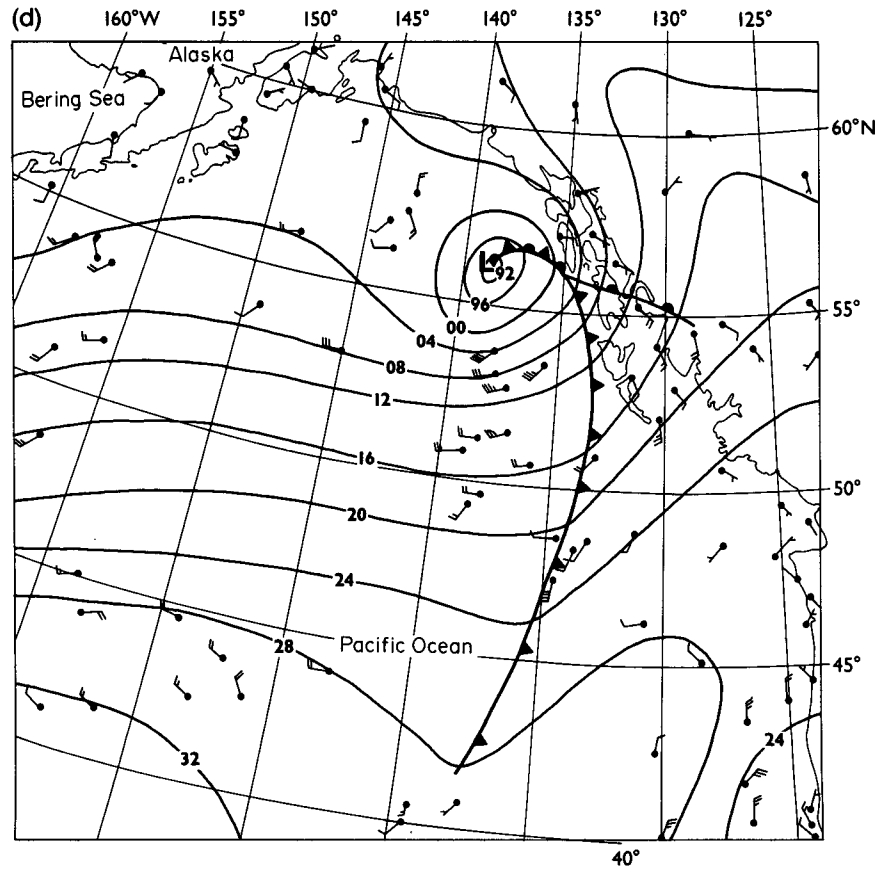

FIG. 11. (*Continued*)

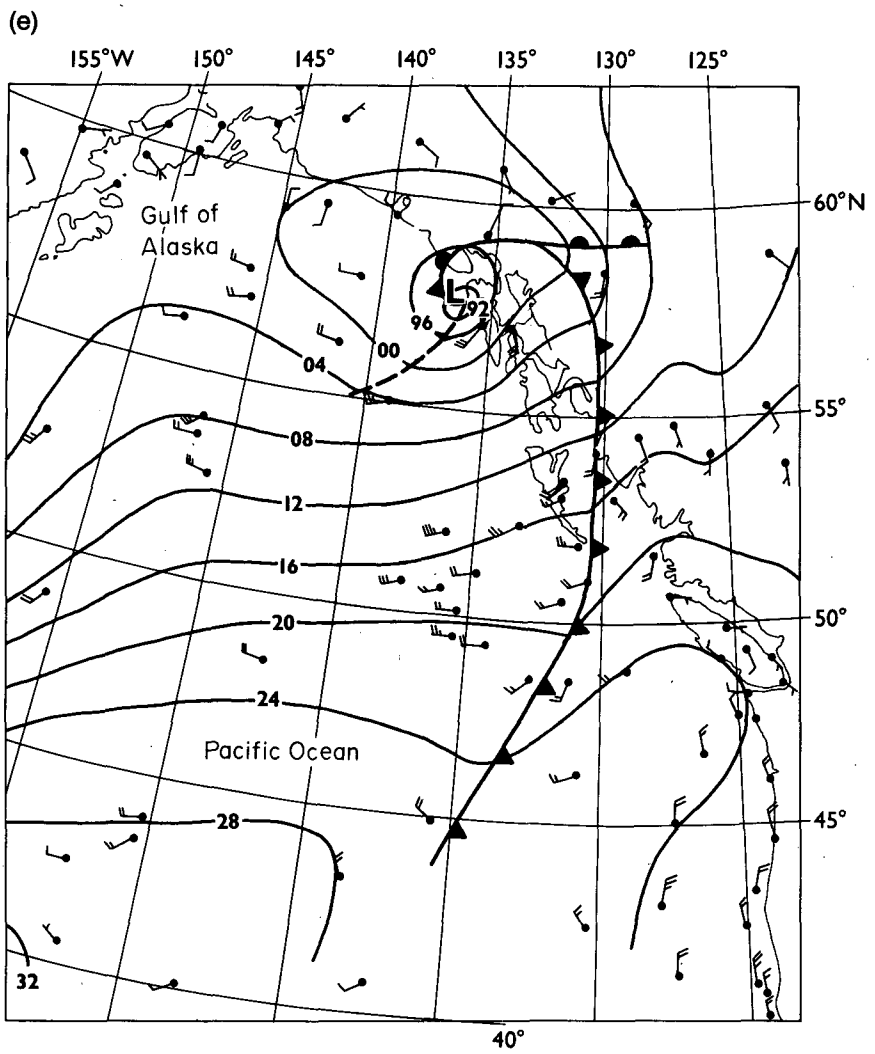

FIG. 11. (*Continued*)

over the depth of the cloud layer are consistent with the predictions of both theories.

CSI predicts zero propagation velocity with respect to the mean wind, and the near neutrality of the atmosphere to CSI (Fig. 5c) may imply CSI adjustment. However, satellite imagery and radar data from the aircraft indicate that the rainbands exhibited a cellular, convective nature as opposed to the continuous lines of more uniform ascent associated with CSI. The layer below ~850 mb was also potentially unstable to upright convection. Bennetts and Ryder (1984) have suggested that symmetric instability may organize convective release by drawing potentially unstable air into the upward branch of symmetric rolls, thus making it convectively unstable.

A wave-CISK mechanism, in which convection is organized by the vertical shear of the horizontal wind, would be expected to lead to significant along-band variations as the satellite observations suggest were present. However, wave-CISK predicts propagation with respect to the mean flow, which was not observed in this case for the more intense rainbands. Since the growth rates for convective instability are much larger than those for either CSI or wave-CISK, convective instability aided by either CSI or wave-CISK probably dominated this case. In the future, increased resolution of the in situ data sampling may help to resolve this question further.

Fluxes of latent and sensible heat were moderately large over the Northern Pacific Ocean and Northern Gulf of Alaska during the time of the aircraft flight. These values resulted in the modification of boundary-layer air as dry, cold arctic air was advected from the Bering Sea over these regions. Fluxes of latent and sensible heat from the sea surface may have contributed to the potential instability found below ~850 mb in

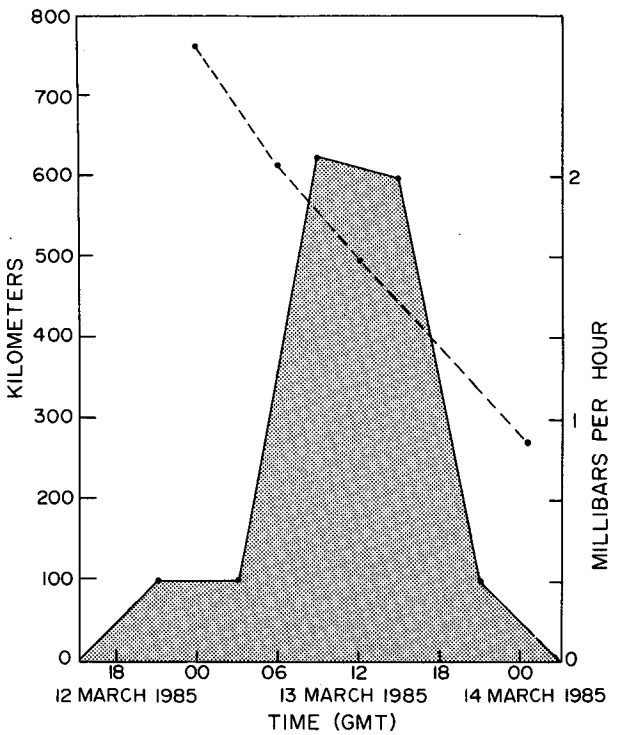

FIG. 12. Rate of sea-level pressure change with time following the storm center (solid contour), and the horizontal distance separating the 500 mb trough axis and the location of the surface low-pressure center (dashed contour).

the cross sections (Fig. 3), the reduced values of Ri at low levels (Table 1) and the low values of the lifted index.

Satellite imagery showed the evolution of several separate comma-cloud or convective systems out of the genesis region on March 13 (labeled A–D in the satellite imagery). The comma-cloud systems exhibited very short wavelengths (~500 km). Calculations of Ri showed the smallest values occurred below ~850 mb and rapidly increased above ~600 mb (Table 1). These observations agree with numerical modeling results showing that mean flows with significantly lower Ri near the surface than aloft, favor higher linear growth rates for small synoptic-scale waves.

As the short-wave trough at 500 mb approached a preexisting polar front, a wave cyclone developed rapidly on the front. Dropwindsonde data showed that convection redistributed moisture and heat in the vertical, ahead of the 500 mb trough axis. As the upper-level trough overtook the surface low-pressure center, this preconditioning may have led to enhanced frontal uplift along the cloud band of the occlusion in a region strongly forced by differential PVA. These factors generated cyclonic vorticity near the surface and may have contributed to the explosive growth of the wave cyclone.

The signature of strong convective activity could be seen along the occlusion cloud band and convective system A in the satellite image for 2300 UTC 13 March (Fig. 8a). During the following 3 hours the southwest end of the occlusion cloud band and convective system A rapidly expanded in areal extent and appeared to merge, developing the characteristic "comma" shape within the larger comma of the wave cyclone in the satellite image for 0200 UTC 14 March (Fig. 8b). Careful tracking of the cloud features showed that the head of the comma cloud developed out of the inner spiral of the occlusion cloud band, while convective system A provided the tail of the comma cloud. Very little response was seen in the surface data at Juneau and Sitka on the SE Alaska panhandle when the initial front associated with the wave cyclone passed. However, when the surface trough of the comma cloud passed, surface data at these locations showed unexpectedly strong winds and a pronounced "V" in the barograph trace.

Model forecasts by NMC's Limited Area Fine Mesh (LFM) model underestimated the deepening of the cyclone. Some of this discrepancy may be accounted for by an underestimate of the amplitude of the 500 mb short-wave trough at 0000 UTC 13 March. Additionally, diabatic effects not properly parameterized in the model may have been important.

This paper highlights the diversity of mesoscale phenomena that exist in polar airmasses over the ocean, and their potential importance to forecasting problems such as rapid cyclogenesis. The value of increased data sampling over data sparse areas to improve analyses

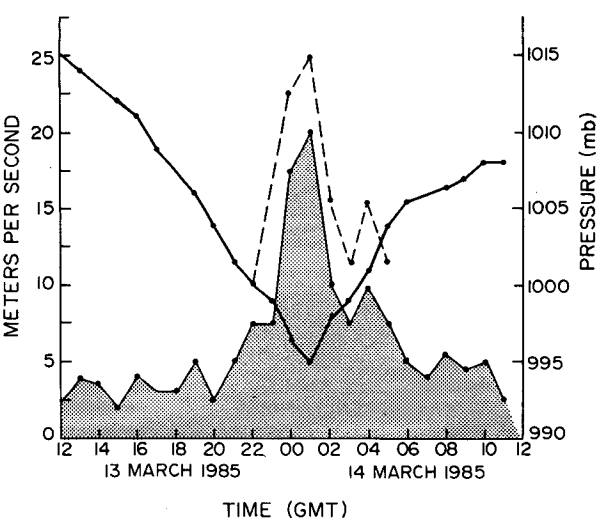

FIG. 13. Hourly barometric surface-pressure and wind-speed data from Juneau, Alaska on 13–14 March 1985. The light solid contour is the average wind speed, dashed contour is the 5 second wind-gust average. The heavy-solid contour is the barometric-pressure trace.

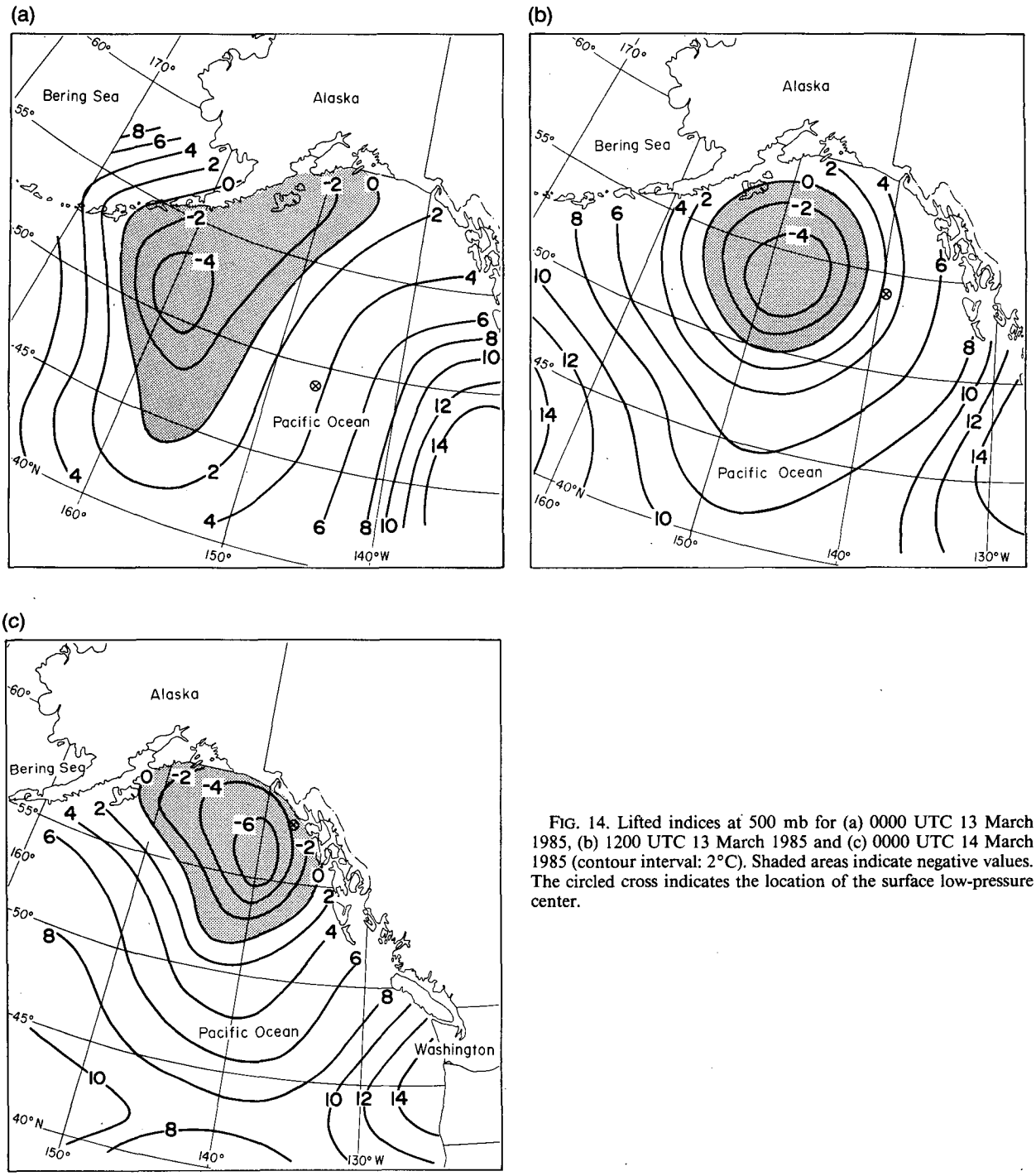

FIG. 14. Lifted indices at 500 mb for (a) 0000 UTC 13 March 1985, (b) 1200 UTC 13 March 1985 and (c) 0000 UTC 14 March 1985 (contour interval: 2°C). Shaded areas indicate negative values. The circled cross indicates the location of the surface low-pressure center.

and numerical forecasts was reinforced in this study. It is clear that progress towards understanding and forecasting these varied phenomena depends on continued research efforts. These efforts need to include: (i) field projects that provide observational data that can document the evolution of various mesoscale phenomena so that theoretical and conceptual models can be developed, and (ii) continued development of mesoscale numerical models to investigate and simulate this evolution.

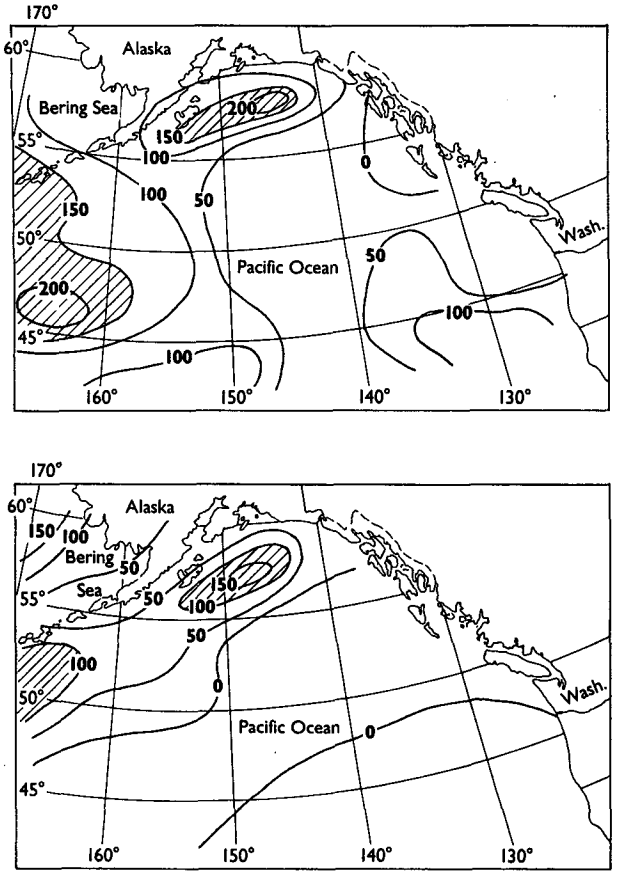

FIG. 15. Surface fluxes for 0000 UTC 13 March 1985 (contour interval: 50 W m^{-2}): (a) latent-heat fluxes (shaded areas indicate upward fluxes > 150 W m^{-2}) and (b) sensible-heat fluxes (shaded areas indicate upward fluxes > 100 W m^{-2}).

REFERENCES

Anderson, R. K., J. P. Ashman, F. Bittner, G. R. Farr, E. W. Ferguson, V. J. Oliver and A. H. Smith, 1969: Application of meteorological satellite data in analysis and forecasting. ESSA Tech. Rep. NESC 51, U.S. Dept. of Commerce, Washington, DC. [NTIS AD-697 022.]

Bennetts, D. A., and B. S. Hoskins, 1979: Conditional symmetric instability; a possible explanation for frontal rainbands. *Quart. J. Roy. Meteor. Soc.*, **105**, 595–602.

——, and P. Ryder, 1984: A study of mesoscale convective bands behind cold fronts. Part I: Mesoscale organization. *Quart. J. Roy. Meteor. Soc.*, **110**, 121–145.

Blumen, W., 1980: On the evolution and interaction of short and long baroclinic waves of the Eady type. *J. Atmos. Sci.*, **37**, 1984–1993.

Browning, K. A., and F. F. Hill, 1985: Mesoscale analysis of a polar trough interacting with a polar front. *Quart. J. Roy. Meteor. Soc.*, **111**, 445–462.

Businger, S., and P. V. Hobbs, 1987: Mesoscale structures of two comma-cloud systems over the Pacific Ocean. *Mon. Wea. Rev.*, **115**, 1908–1928.

Carleton, A. M., 1985: Satellite climatological aspects of the polar low and "instant occlusion." *Tellus*, **37**, 433–450.

Duncan, C. N., 1977: An investigation of polar lows. *Quart. J. Roy. Meteor. Soc.*, **103**, 255–268.

Durran, D. R., and J. B. Klemp, 1982: On the effects of moisture on the Brunt-Väisälä frequency. *J. Atmos. Sci.*, **39**, 2152–2158.

Eady, E. T., 1949: Long waves and cyclone waves. Tellus, **1**, 33–52.

Farrell, B. F., 1982: Initial growth of a disturbance in a baroclinic flow. *J. Atmos. Sci.*, **39**, 507–517.

——, 1984: Modal and nonmodal baroclinic waves. *J. Atmos. Sci.*, **41**, 668–673.

Gall, R. L., 1976: The effects of latent heat release in growing baroclinic waves. *J. Atmos. Sci.*, **33**, 1686–1701.

Holton, J. R., 1979: *Introduction to Dynamic Meteorology.* Academic Press, 391 pp.

Hoskins, B. J., M. E. McIntyre and A. W. Robertson, 1985: On the use and significance of isentropic potential vorticity maps. *Quart. J. Roy. Meteor. Soc.*, **111**, 877–946.

Locatelli, J. D., P. V. Hobbs and J. A. Werth, 1982: Mesoscale structures of vortices in polar air streams. *Mon. Wea. Rev.*, **110**, 1417–1433.

Mansfield, D. A., 1974: Polar lows: The development of baroclinic disturbances in cold air outbreaks. *Quart. J. Roy. Meteor. Soc.*, **100**, 541–554.

Mullen, S. L., 1979: An investigation of small synoptic scale cyclones in polar airstreams. *Mon. Wea. Rev.*, **107**, 1636–1647.

——, 1983: Explosive cyclogenesis associated with cyclones in polar airstreams. *Mon. Wea. Rev.*, **111**, 1537–1553.

Newton, C. W., 1950: Structure and mechanisms of the pre-frontal squall line. *J. Meteor.*, **7**, 210–222.

Orlanski, I., 1986: Localized baroclinicity: A source for mesoα cyclones. *J. Atmos. Sci.*, **43**, 2857–2885.

——, and L. Polinsky, 1984: Predictability of mesoscale phenomena. *Proc. Second Int. IAMP/WMO/ESS Symp. on Nowcasting*, Norrköping, Sweden, 271–280.

Parsons, D. B., and P. V. Hobbs, 1983: The mesoscale and microscale structure and organization of clouds and precipitation in midlatitude cyclones, XI: Comparisons between observational and theoretical aspects of rainbands. *J. Atmos. Sci.*, **40**, 2377–2397.

Petterssen, S., and S. J. Smebye, 1971: On the development of extratropical cyclones. *Quart. J. Meteor. Soc.*, **97**, 457–482.

Reed, R. J., 1979: Cyclogenesis in polar airstreams. *Mon. Wea. Rev.*, **107**, 38–52.

——, and M. D. Albright, 1986: A case study of explosive cyclogenesis in the Eastern Pacific. *Mon. Wea. Rev.*, **114**, 2297–2319.

——, and W. Blier, 1986a: A case study of comma cloud development in the Eastern Pacific. *Mon. Wea. Rev.*, **114**, 1681–1695.

——, and ——, 1986b: A further case study of comma cloud development in the Eastern Pacific. *Mon. Wea. Rev.*, **114**, 1696–1708.

Sanders, F., and J. R. Gyakum, 1980: Synoptic-dynamic climatology of the "Bomb". *Mon. Wea. Rev.*, **108**, 1589–1606.

Satyamurti, P., V. B. Rao and A. D. Moura, 1982: Subsynoptic-scale baroclinic instability. *J. Atmos. Sci.*, **39**, 1052–1061.

Staley, D. O., and R. L. Gall, 1977: On the wavelength of maximum baroclinic instability. *J. Atmos. Sci.*, **34**, 1679–1688.

Stone, P. H., 1966: On non-geostrophic baroclinic stability. *J. Atmos. Sci.*, **23**, 390–400.

Sun, W. Y., 1978: Stability analysis of deep cloud streets. *J. Atmos. Sci.*, **35**, 466–483.

——, 1984: Rainbands and symmetric instability. *J. Atmos. Sci.*, **41**, 3412–3426.

Sutcliffe, R. C., 1947: A contribution to the problem of development. *Quart. J. Roy. Meteor. Soc.*, **73**, 370–383.

Tokioka, T., 1973: A stability study of medium-scale disturbances with inclusion of convective effects. *J. Meteor. Soc. Japan*, **51**, 1–9.

Zillman, J. W., and P. G. Price, 1972: On the thermal structure of mature southern ocean cyclones. *Aust. Meteor. Mag.*, **20**, 34–48.